CHEMISTRY OF MATERIALS

ARTICLE

pubs.acs.org/cm

Origin of the High Upconversion Green Luminescence Efficiency in β-$NaYF_4$:2%Er^{3+},20%Yb^{3+}

C. Renero-Lecuna,* R. Martín-Rodríguez, and R. Valiente

Departamento de Física Aplicada, MALTA CONSOLIDER Team, Universidad de Cantabria, Santander 39005, Spain and Centro Asociado de Condiciones Extremas, ICMA-CSIC, Santander 39005, Spain

J. González and F. Rodríguez

DCITIMAC, MALTA CONSOLIDER Team, Facultad de Ciencias, Universidad de Cantabria, 39005, Santander, Spain

K. W. Krämer and H. U. Güdel

Department of Chemistry and Biochemistry, University of Bern, 3012 Bern, Switzerland

ABSTRACT: Site-selective spectroscopy in hexagonal β-$NaYF_4$:Er^{3+},Yb^{3+} has revealed different environments for Er^{3+} ions (multisite formation). The low-temperature $^4S_{3/2} \rightarrow {}^4I_{15/2}$ Er^{3+}green emission depends on the excitation wavelength associated with the $^4F_{7/2}$ Er^{3+} level. We have studied the effect of hydrostatic pressure on the green, red, and blue Er^{3+} emission upon NIR excitation at ~980 nm, in order to establish the role played by energy resonance conditions and the multiple Er^{3+} sites due to the disordered structure for the upconversion (UC) process (energy tuning). The variation of photoluminescence spectra and lifetimes as a function of pressure and temperature reveals that the origin of the high green UC efficiency of the β-$NaYF_4$:Er^{3+},Yb^{3+} compound is mainly due to the multisite distribution, and the low phonon energy of the host lattice.

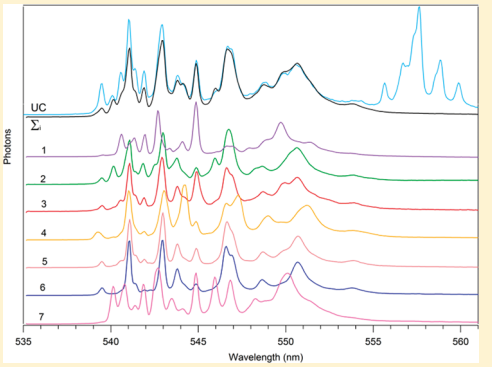

KEYWORDS: upconversion, $NaYF_4$: Er^{3+}, Yb^{3+}, high pressure, luminescence, multisites, site selective spectroscopy

INTRODUCTION

Upconversion (UC) processes consist of the transformation of two or more low-energy photons (typically in the infrared (IR) region) to one emitted higher-energy photon (in the ultraviolet−visible light (UV−vis) region). β-$NaYF_4$ codoped with Er^{3+} and Yb^{3+} is one the most widely used compounds for many different applications in optical fibers,[1] solar cell enhancement,[2] laser host materials, IR counter, or even as security ink or a magnetic field detector;[3,4] it also has biological applications in immunoassay detectors,[5] bioimaging,[6] intracellular imagine,[7] nanothermometer,[8] and displays.[9]

Although its exceptional properties as UC phosphor have been known since the 1970s,[10] the synthesis of colloidal nanoparticles[11] with potential applications in biology, opto-electronic devices, solar cells, sensors, etc., has further increased the relevance of this material. Since then, an increasing number of papers has appeared every year. In fact, β-$NaYF_4$ microcrystals codoped with 2% Er^{3+} and 20% Yb^{3+} show the most-efficient green UC phosphors to date.[12]

In order to improve its UC efficiency, different synthesis routes together with new complementary techniques for nanoparticle characterization have been proposed. However, despite this effort, the microscopic origin of the high UC luminescence efficiency remains unknown. Because of this, three distinctive structural factors seem to account for its high UC efficiency: (1) the high disordered structure due to cation (Na^+) distribution;[13] (2) the significant low phonon energy of the host lattice for fluorides (~370 cm^{-1});[12,14] and (3) the highly resonant energy transfer between Yb^{3+} ($^2F_{5/2}$) and Er^{3+} ($^4I_{11/2}$) levels. Therefore, knowledge of how these three factors work is essential to understand the exceptional UC-phosphor capability of this material. Furthermore, unraveling the causes of its high UC efficiency can be crucial for increasing material reliability and its applications.

We have carried out site-selective and time-resolved spectroscopy at different temperatures (17, 100, and 300 K) and pressure (up to 30 GPa) in microcrystalline powder, in order to achieve these goals. In particular, attention is focused on the green spectral region associated with the main transition $^4S_{3/2} \rightarrow {}^4I_{15/2}$. Along this work, we will show that the application of these techniques has been essential to demonstrate the influence of the three previously mentioned factors in the UC performance of this material.

Received: February 9, 2011
Revised: June 9, 2011
Published: July 06, 2011

EXPERIMENTAL METHOD

Microcrystalline powders of β-$NaYF_4$:2%Er^{3+},20%Yb^{3+} were synthesized using the route that has been described elsewhere.[15] The average size of these microcrystals was ~2 μm.

Time-resolved excitation and emission spectroscopies were carried out with an Optical Parametric Oscillator (OPO) system (Vibrant II, Opotek) for excitation and a Horiba−Jobin-Yvon intensified charge-coupled device (CCD) (iCCD S20 Gen II) for photoluminescence (PL) detection. The spectral line width of the OPO pulsed laser was smaller than 7 cm^{-1}, below the homogeneous peak width of the different Er^{3+} sites. The light was dispersed with a TRIAX320 monochromator (1200 grooves/nm; blazed at 500 nm).

Unpolarized confocal micro-Raman scattering measurements were performed at room temperature in a triple monochromator (Jobin-Yvon, Model T64000) in subtractive-mode backscattering configuration, equipped with a liquid-N_2 cooled CCD detector. For excitation, the 647-nm line of an Ar^+−Kr^+ laser was focused on the sample by means of a 100× objective, while the laser power was kept below 40 mW, in order to avoid laser-heating effects. The laser spot was 2 μm in diameter, and the spectral resolution was better than 2 cm^{-1}. The accumulation time was typically three collections of 1 s. The spectrum was fitted to Lorentzian profiles.

High-pressure experiments as a function of temperature in the 0−30 GPa range were performed in a cryogenic diamond anvil cell (cryoDAC from EasyLab), together with a closed-cycle He cryostat (ARS).

Temporal evolution of the direct or UC luminescence intensity was achieved after light dispersion by a 0.5-m single monochromator (Chromex 500IS/SM) with a photomulplier (Model R928, Hamamatsu) and a multichannel scaler (Stanford Research, Model SR-430).

All spectra were corrected for the instrumental response.[16]

RESULTS AND DISCUSSION

β-$NaYF_4$ is related to the $NaCaY(F,Cl)_6$ (gagarinite) and UCl_3 structural families. Recently, a controversy has arose about which space group, either $P\bar{6}$ or $P6_3/m$, better describes the β-$NaYF_4$ (Z = 1.5) phase.[10,13−15,17−19]

Although the $P6_3/m$ model requires less structural parameters, it is clearly insufficient. The $P\bar{6}$ space group accounts correctly for β-$NaYF_4$. This was proven, e.g., by single crystal X-ray diffraction,[10,13] polarized optical absorption,[13] Raman spectroscopy,[14] and second harmonic generation.[19] The latter requires an acentric space group and therefore clearly excludes $P6_3/m$. The average structure of β-$NaYF_4$ displays a strong cation disorder[10,13] (see Figure 1). The trivalent rare-earth ions occupy site (1a) and half of site (1f). The Na^+ ions occupy the other half of site (1f) and half of the (2h) site. Both rare-earth sites show a coordination number of nine in the shape of a tricapped trigonal prism. The point symmetry of both (1a) and (1f) sites is C_{3h} in the average structure. However, the detailed analysis of the diffuse X-ray scattering, as well as polarized absorption spectra, revealed that the actual point symmetry of the (1a) site is much lower in a microscopic structural model.[13] The cation disorder on the (1f) site invokes local anion displacements, i.e., slightly longer Na−F and shorter Y−F distances (see Figure 1). Those reduce the actual symmetry of the (1a) site by moving the three capping F^- ions up or down along the c-axis. Statistically, these movements are unequal yielding symmetry reduction and a vast site distribution. Most centers have C_1 symmetry, whereas a small percentage of them only can maintain the higher C_3 symmetry.

The RT Raman spectrum of β-$NaYF_4$:2%Er^{3+},20%Yb^{3+} was taken in subtractive mode using 647-nm light in order to avoid unwanted luminescence (Figure 2). It shows seven inhomogeneously broadened peaks, labeled from 1 to 7. Table 1 collects the

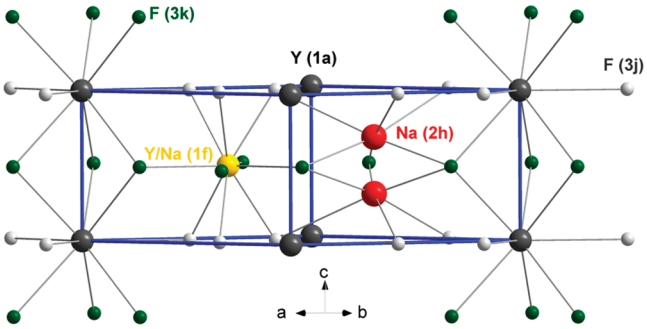

Figure 1. Crystal structure of β-$NaYF_4$, space group $P\bar{6}$, Z = 1.5. The (1a) site is occupied by Y, the (1f) site is half occupied by Y and half by Na, (2h) site is half occupied by Na and half by vacancies. F occupies the (3k) and (3j) sites. The microscopic displacement of F on the (3j) sites away from Na on the (1f) site and toward Y on the (1f) site breaks the symmetry of the (1a) site. This microscopic displacement is not shown in this average structure.

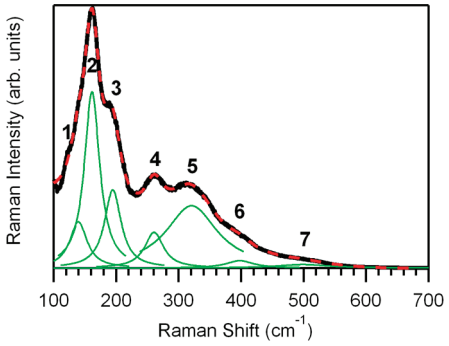

Figure 2. Room-temperature (RT) Raman spectrum of β-$NaYF_4$:Er^{3+}, Yb^{3+} micropowders in backscattering configuration. The phonon energies are collected in Table 1. (λ_{ex} = 647 nm. Red and green lines represent the Lorentzian fitting.)

position and the full-width at half-maximum (fwhm) of the Lorentzian fitted peaks. The line shape is inhomogeneously broadened due to the disordered structure.

By comparing the Raman spectra of Figure 2 and that for the undoped β-$NaYF_4$ given in ref 9, we conclude that, in general, there is fair agreement between present data and those obtained in the $NaLnF_4$ (Ln = La, Ce, Pr, Sm, Eu, and Gd) series.[14] This probes that the highest phonon energy in this material is ~500 cm^{-1}. This fact makes this host material a very good one, in terms of luminescence efficiency according to the energy gap law that establishes the relevance of the multiphonon de-excitation processes in lanthanide compounds.

Figure 3 shows the RT absorption (Figure 3a) and emission spectra under $^4F_{7/2}$ Er^{3+} (Figure 3b) and $^2F_{5/2}$ Yb^{3+} (Figure 3c) excitation of β-$NaYF_4$:2%Er^{3+},20%Yb^{3+}. The strongest absorption band ~1000 nm, corresponding to the $^2F_{7/2} \rightarrow {}^2F_{5/2}$ Yb^{3+} transition, appears broadened at RT. The remainder absorption peaks are due to f-f transitions from the ground-state $^4I_{15/2}$ to excited states of Er^{3+} ions, which have been assigned according to Dieke's diagram (see Figure 4). Figure 3b shows the Er^{3+} emission spectrum in the visible region after direct excitation at 487.5 nm ($^4F_{7/2}$ multiplet). The spectrum is dominated by the $^4S_{3/2} \rightarrow {}^4I_{15/2}$ transition in the green spectral region (540−550 nm). In addition, the $^4F_{9/2} \rightarrow {}^4I_{15/2}$ red emission and the

dx.doi.org/10.1021/cm2004227 |Chem. Mater. 2011, 23, 3442–3448

Table 1. Energy, Full Width at Half Maximum, and Intensity of the Seven Lorentzian Peaks Fitted to the Raman Spectrum of Figure 2[a]

	Peak No. 1	Peak No. 2	Peak No. 3	Peak No. 4	Peak No. 5	Peak No. 6	Peak No. 7
position (cm^{-1})	139	161	194	261	321	398	500
full width at half maximum, fwhm (cm^{-1})	33	30	32	37	100	54	104
intensity, I (arb. units)	1626	6176	2748	1257	2186	262	126

[a] The energy corresponds to the phonon energy of the host lattice.

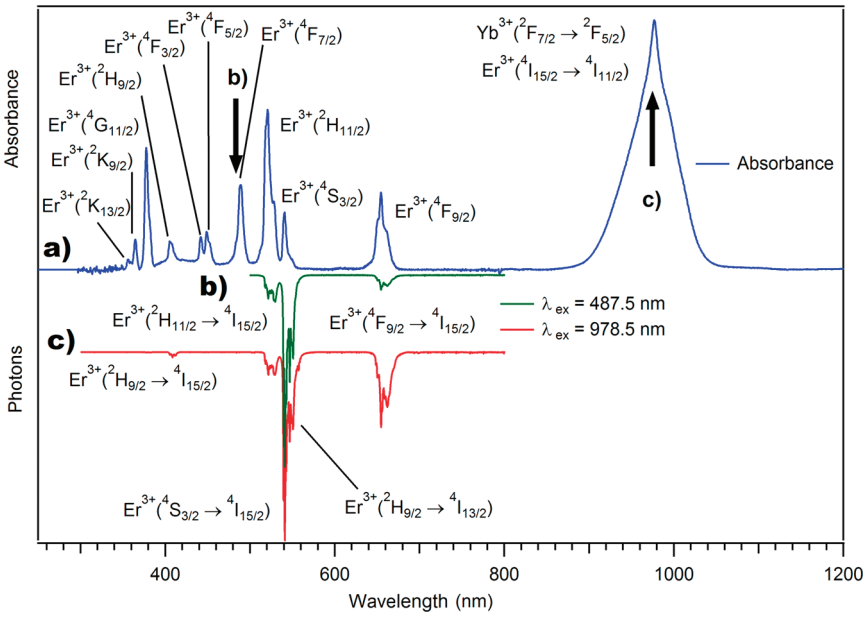

Figure 3. RT absorption (a) direct (b) and UC luminescence (c) spectra of β-$NaYF_4$:2%Er^{3+},20%Yb^{3+} excited at 487.5 nm ($^4F_{7/2}$) and 978.5 nm ($^2F_{5/2}$) (arrows), respectively, taken at ambient pressure. The labels for the emission and absorption spectra show the states involved in the electronic transition.

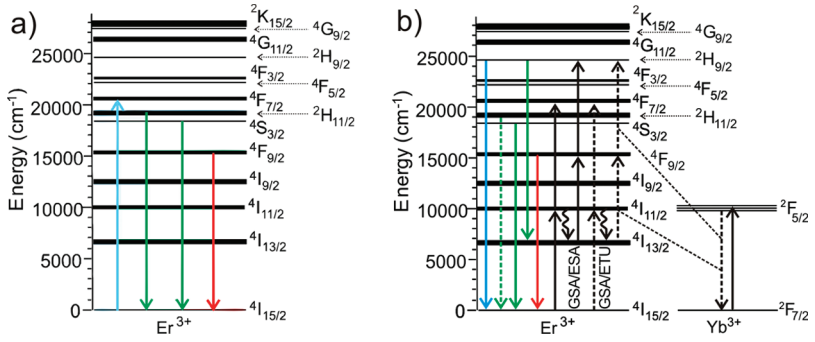

Figure 4. Energy level diagrams for (a) direct Er^{3+} excitation and (b) Er^{3+}−Yb^{3+} system, showing the energy transfer upconversion (ETU) processes responsible for the VIS emission after NIR excitation into the $^2F_{5/2}$ multiplet of Yb^{3+}. The colors represent the type of radiation of the emitted photons. Only visible emissions are shown.

thermalized $^2H_{11/2} \rightarrow {}^4I_{15/2}$ transition are also observed (Figures 3b and 4a). The UC spectrum in Figure 3c is obtained upon Yb^{3+} ($^2F_{5/2}$) excitation and energy transfer to Er^{3+}. The main observed transitions are essentially the same ones as in Figure 3b. According to Figure 4b, the remarkable intensity rise of the red emission, compared to direct Er^{3+} excitation, is due to the population of $^4F_{9/2}$ via energy transfer after $^4I_{11/2} \rightarrow {}^4I_{13/2}$ nonradiative relaxation and cross-relaxation between Er^{3+}-excited levels. Besides, a new band appears at ∼420 nm (blue emission) due to de-excitation from $^2H_{9/2}$. This level is populated through multistep photon absorption as indicated in Figure 4b. Apart from the blue emission, it also generates new green emission peaks at ∼557 nm by de-excitation to the $^4I_{13/2}$ level.

The energy level schemes of Er^{3+} and Yb^{3+} in β-$NaYF_4$ (Figure 4) show the main transitions involved in absorption and emission, as well as the dominant UC processes observed upon excitation at 978.5 nm. The blue arrow in Figure 4a indicates the excitation energy required to populate the

dx.doi.org/10.1021/cm2004227 |Chem. Mater. 2011, 23, 3442–3448

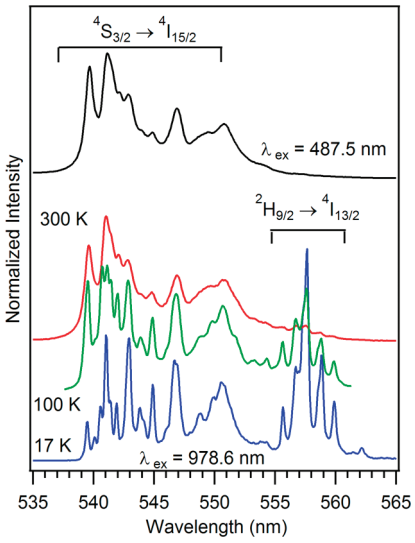

Figure 5. Direct (upper trace) and UC luminescence spectra of the $^4S_{3/2} \rightarrow {}^4I_{15/2}$ transition in β-$NaYF_4$:2%Er^{3+},20%Yb^{3+}. The temperature dependence of the UC luminescence is given at 300, 100, and 17 K.

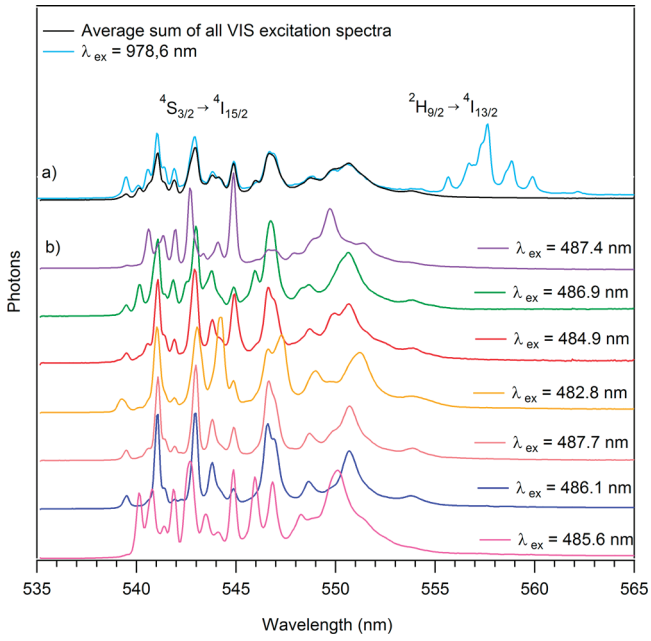

Figure 6. (a) UC emission spectrum of β-$NaYF_4$:2%Er^{3+},20%Yb^{3+} (blue), compared with the sum of all $^4F_{7/2}$ - Er^{3+} excited emission spectra of (b); and (b) emission spectra obtained at different direct excitation wavelengths into the $^4F_{7/2}$ multiplet of Er^{3+} at 17 K and ambient pressure. The emissions correspond to $^4S_{3/2} \rightarrow {}^4I_{15/2}$ and $^2H_{9/2} \rightarrow {}^4I_{13/2}$ transitions.

$^4F_{7/2}$ Er^{3+} at 487.5 nm, giving rise to the three emission bands observed in Figure 3b. The black solid arrow in Figure 4b shows the excitation energy populating the $^2F_{5/2}$ multiplet of Yb^{3+}. The black dashed arrows represent the multistep energy transfer processes responsible for the ETU mechanism in the material. The colored arrows show different emission transitions of Er^{3+} appearing in the UC spectrum of Figure 3c. The dashed lines show the resonant energy transfer mechanism between Yb^{3+} ($^2F_{5/2}$) and Er^{3+} ($^4I_{11/2}$), which is responsible for the UC high-energy level ($^4F_{7/2}$) and ($^2H_{9/2}$) populations, and, hence, the blue Er^{3+} emission $^2H_{9/2} \rightarrow {}^4I_{15/2}$ at ~420 nm appearing in the UC spectrum. Moreover, new emission peaks appear at ~557 nm in the green emission band. They are due to the $^2H_{9/2} \rightarrow {}^4I_{13/2}$ transition as evidenced through lifetime measurements (not shown here). In fact, these measurements indicate that these new peaks arise only from $^2H_{9/2}$ and are different from the green emission associated with the $^4S_{3/2} \rightarrow {}^4I_{15/2}$ transition.

Hereafter, we aim to study the green Er^{3+} emission band under visible (vis) and near-infrared (NIR) excitation, since it exhibits some unusual features, particularly the presence of new peaks at ~557 nm upon NIR illumination, or the reliable dependence of the emission spectrum with the excitation wavelength in the vis range at low temperature.

By comparing the vis and UC emission spectra in the green spectral region (Figure 5), we notice the appearance of some temperature-dependent peaks in the UC spectra at ~557 nm. Their intensity increases upon cooling but is practically quenched at 300 K. These peaks correspond to the $^2H_{9/2} \rightarrow {}^4I_{13/2}$ transition (Figure 4b), which is induced upon IR excitation after $^2H_{9/2}$ population via three photon process. Direct excitation into Er^{3+} ($^4F_{7/2}$) yields $^4S_{3/2}$ population and no evidence of $^2H_{9/2}$ population is detected via consecutive resonant energy transfer or excited state absorption at ~557 nm in the upper trace of Figure 5. Therefore, neither blue emission ($^2H_{9/2} \rightarrow {}^4I_{15/2}$) nor 557 nm emission ($^2H_{9/2} \rightarrow {}^4I_{13/2}$) is expected upon direct Er^{3+} excitation at 487.5 nm, since $^2H_{9/2}$ is not populated.

An interesting excitation-wavelength-dependent phenomenon occurs in the emission spectrum below 100 K, depending on the excitation wavelength, through direct Er^{3+} excitation. A distinct emission spectrum is observed upon excitation at different wavelengths between 482 and 488 nm. The excitation spectrum becomes well-resolved showing different excitation peaks between 482 and 488 nm, thus indicating multisite presence in β-$NaYF_4$:2% Er^{3+},20% Yb^{3+}. This is illustrated in Figure 6, where different emission spectra are observed at different excitation wavelengths. The slight spectral variations and the peak shifts observed in each emission spectrum reveal that Er^{3+} is subject to different crystal-field environments associated with the disordered structure mentioned above. The fact that the UC spectrum can be fairly well reproduced by the sum of all individual contributions from the Er^{3+} multisites is noteworthy (Figure 6a). However, this wavelength-excitation dependence is not observed upon NIR excitation in $^2F_{7/2} \rightarrow {}^2F_{5/2}$ Yb^{3+}. Instead, the UC emission spectrum taken upon Yb^{3+} excitation is essentially the same at 17 K and RT. These features clearly indicate that all Er^{3+} ions are activated after Yb^{3+} excitation (UC) via an ETU process, whereas visible light can only excite selected Er^{3+} sites, leading to excitation-wavelength-dependent emission spectra for Er^{3+}. Upon increasing the temperature to >100 K, the site tuneability through selective wavelength excitation disappears and the resulting spectrum is the average of the multisite Er^{3+} emissions, as can be seen in Figure 5.

Figure 7 shows the correlation between the excitation wavelength (two-dimensional (2D) image, *x*-axis) and the emission wavelength (2D image, *y*-axis) when the sample is excited into the $^4F_{7/2}$ Er^{3+} multiplet. This plot is relevant to demonstrate multisite spectra. Note that the intensity maxima correspond to the bright white color and change their position along the emission *y*-axis when the excitation energy varies. Because of the different Er^{3+} environment, the *x*,*y*-intensity plot shows an irregular pattern,

dx.doi.org/10.1021/cm2004227 |*Chem. Mater.* 2011, 23, 3442–3448

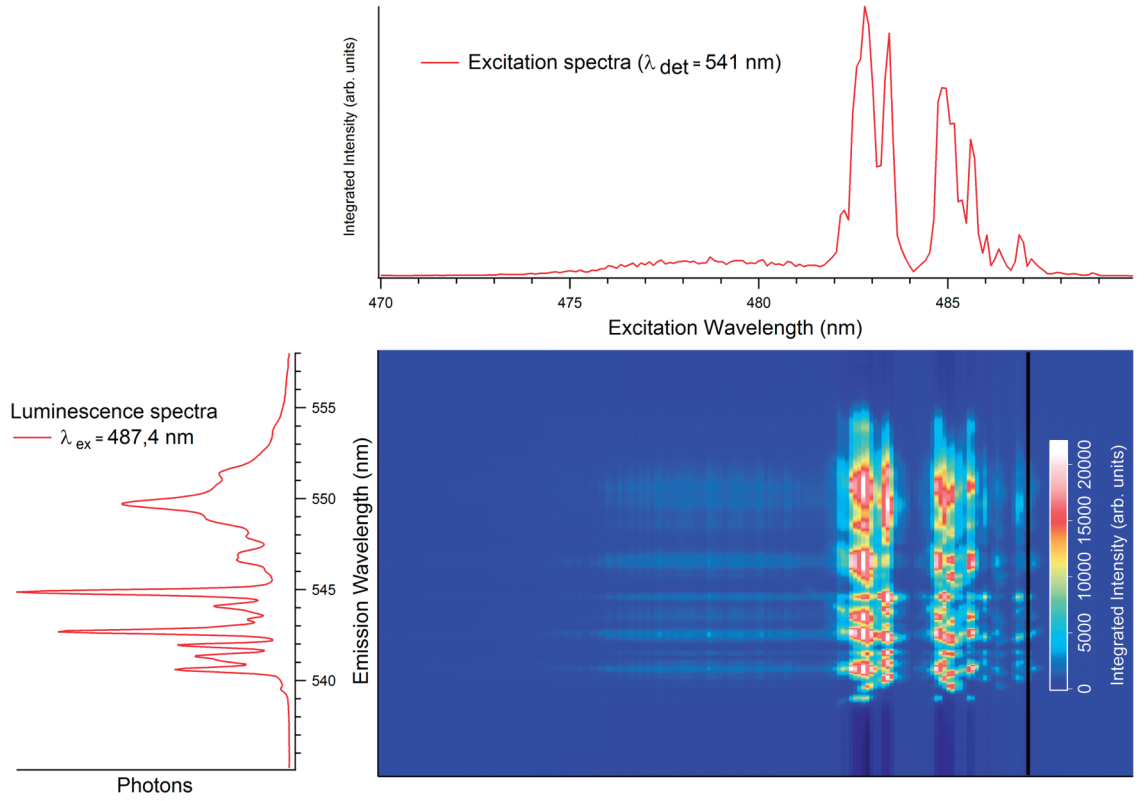

Figure 7. Visible (vis) excitation and emission spectra of β-$NaYF_4$:2%Er^{3+},20%Yb^{3+}. The upper spectrum shows the integrated intensity from the excitation spectra corresponding to emissions from 535 nm to 565 nm. The left-side plot shows the emission spectrum in the green region at ~540 nm upon vis excitation (487.4 nm) at 17 K and ambient pressure. The 2D picture consists of 230 emission spectra (each one obtained at different excitation wavelengths). Horizontal and vertical wavelength scales in the 2D picture correspond to the same one given for the attached spectra. The *x*- and *y*-axes represent the excitation and emission wavelengths, respectively.

which is better resolved at low temperatures; this is the fingerprint for multisite formation. At RT, an average homogeneous emission pattern is observed due to thermal peak broadening (see Figure 5). Figure 7 results an excellent tool for detecting multisites. This result contrasts with those reported by Aebischer et al.[13] in the less-disordered $NaGdF_4$:Er^{3+},Yb^{3+}, where they only report the presence of two different sites.

Opposite to this behavior, UC luminescence via NIR excitation into $^2F_{7/2} \rightarrow {}^2F_{5/2}$ (Yb^{3+}) only shows one emission at low temperature. The UC phenomenon is not sensitive to the presence of multisites, since all sites are activated by ETU from Yb^{3+}; therefore, no emission or excitation spectral variation is expected via UC, irrespective of whether we are dealing with a single-site or multisite systems.

Figure 8 shows the time evolution of the RT UC luminescence $^4S_{3/2} \rightarrow {}^4I_{15/2}$ Er^{3+} in β-$NaYF_4$:2%Er^{3+},20%Yb^{3+} after 8-ns pulsed excitation at 978.6 nm. The fast intensity rise followed by the slow decay clearly indicates a pure ground-state absorption/energy transfer upconversion process (GSA/ETU).

The β-$NaYF_4$:2% Er^{3+},20% Yb^{3+} sample has also been studied under different conditions of pressure and temperature. We observed that the measured PL lifetimes under NIR and vis excitation (not shown here) decrease when temperature increases. The same occurs when the pressure increases. This accompanies a reduction of emission intensity when either the temperature or pressure increases. This is observed for all the excitation wavelengths studied.

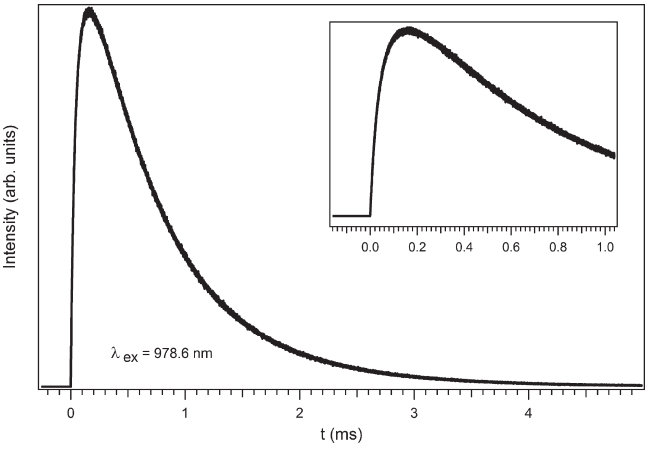

Figure 8. Time evolution of the RT green $^4S_{3/2} \rightarrow {}^4I_{15/2}$ UC emission at ambient pressure (λ_{ex} = 978.6 nm, and pulse repetition rate = 10 Hz).

Figure 9 illustrates the effect of pressure on the UC emission spectra in β-$NaYF_4$:2%Er^{3+},20%Yb^{3+}. First, note that the reduction of emission intensity is due to the pressure-induced detuning between the resonant levels of the Er^{3+} ($^4I_{11/2}$) and the Yb^{3+} ($^2F_{7/2}$). Second, there is an increase of the green-to-red intensity ratio with pressure in the entire temperature range (17−300 K), as well as a reduction of the blue-to-green intensity ratio. Also, the intensity of the new peaks at ~557 nm decreases with

dx.doi.org/10.1021/cm2004227 |*Chem. Mater.* 2011, 23, 3442–3448

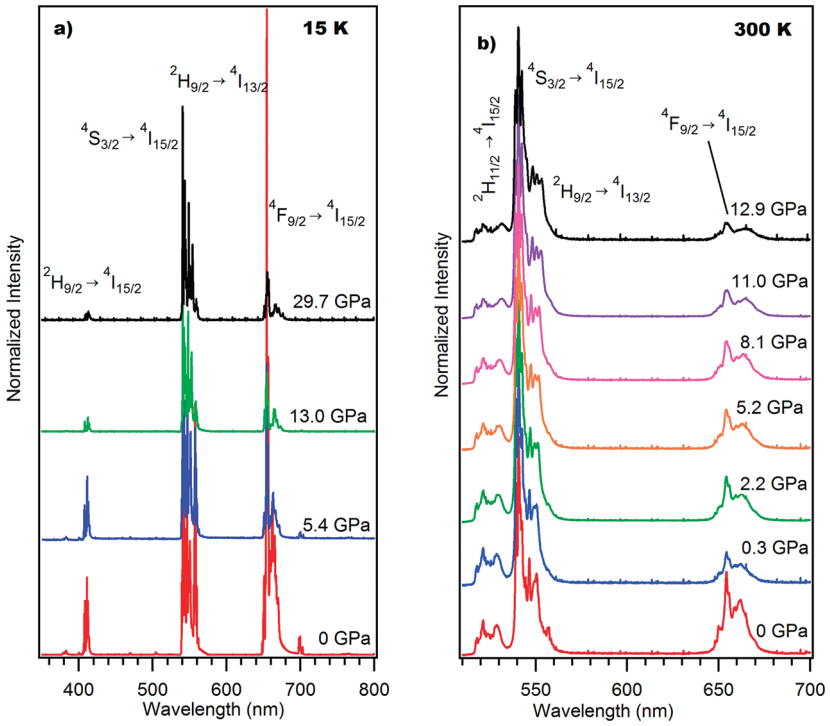

Figure 9. UC emission spectra of the β-$NaYF_4$:2%Er^{3+},20%Yb^{3+} under different pressure conditions: (a) 15 K and (b) RT. All the spectra were normalized to the most intense line of the $^4S_{3/2} \rightarrow {}^4I_{15/2}$ transition in both panels a and b. All excitation wavelengths are at ~978 nm.

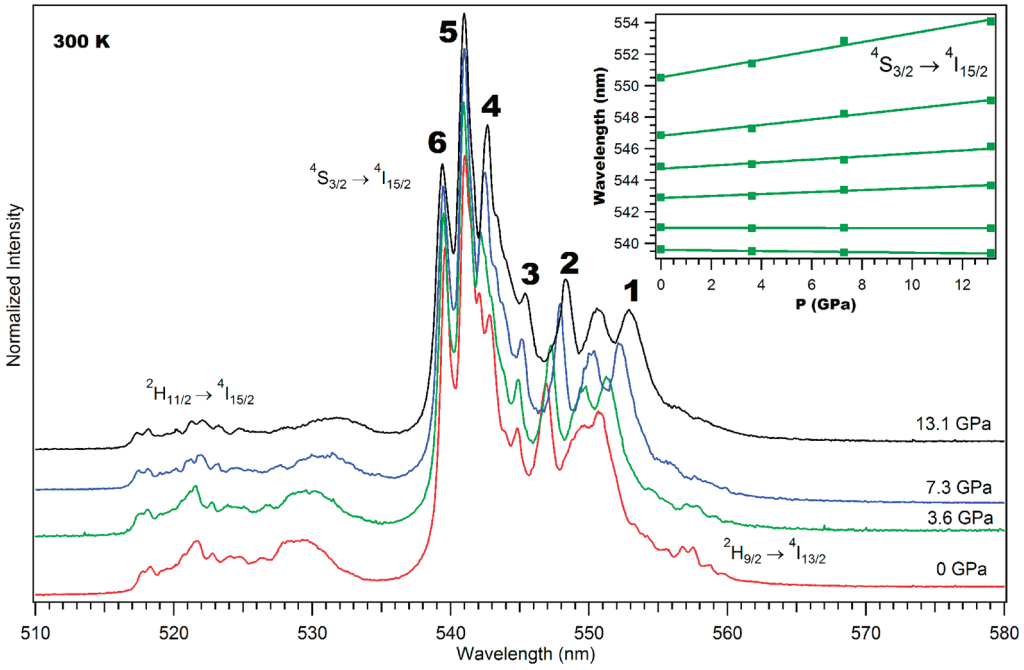

Figure 10. Pressure dependence of the RT UC emission of β-$NaYF_4$:2%Er^{3+},20%Yb^{3+} in the green spectral region; $^2H_{11/2} \rightarrow {}^4I_{15/2}$ (centered at 525 nm), $^4S_{3/2} \rightarrow {}^4I_{15/2}$ (at ~550 nm) and $^2H_{9/2} \rightarrow {}^4I_{13/2}$ (at ~557 nm) emission bands. The inset shows the wavelength shifts with pressure of selected peaks labeled from 1 to 6. The lines are least-squares fits. All excitation wavelengths are at ~978 nm.

pressure. Actually, the green-to-red intensity ratio, corresponding to transitions from $^2H_{11/2}$+$^4S_{3/2}$ and $^4F_{9/2}$ to the ground state, respectively, is a fingerprint for the relevance of nonradiative processes in the Er^{3+}−Yb^{3+} doubly doped systems. As illustrated in Figure 9, its variation reveals that $^4S_{3/2} \rightarrow {}^4I_{15/2}$ and $^2H_{11/2} \rightarrow {}^4I_{15/2}$ transitions approach each other when the pressure increases, leading to a reduction of the energy gap between the thermalized $^2H_{11/2}$ and $^4S_{3/2}$ levels. Also, the

dx.doi.org/10.1021/cm2004227 |*Chem. Mater.* 2011, 23, 3442–3448

intensity of $^2H_{11/2} \rightarrow {}^4I_{15/2}$ drastically decreases with pressure and almost disappears at 13 GPa. We associate the green-to-red intensity ratio increase with pressure to a detuning of the GSA/ETU $^2I_{13/2} \rightarrow {}^2F_{9/2}$ resonance, whereas the green emission is not affected. In addition, we observe an important decrease of the $^2H_{9/2} \rightarrow {}^4I_{15/2}$ blue UC emission intensity with pressure (Figure 9a), which is ascribed to nonradiative relaxation from $^2H_{9/2}$ to lower-lying excited levels, because of both an increase in phonon energy and a decrease in the $^2H_{9/2} - {}^4F_{3/2}$ energy gap.

Another interesting feature is the pressure-induced peak shift in the $^4S_{3/2} \rightarrow {}^4I_{15/2}$ transition upon NIR excitation. In general, the band redshifts with pressure, although the individual peak-shift rate does not follow the general trend of the overall band, as shown in Figure 10. Unlike peaks 1−4, the shift rate of peaks 5 and 6 is negative (blue-shift) and very small. This different behavior reveals that the level splitting in the ground ($^4I_{15/2}$) and excited states ($^4S_{3/2}$) by the Stark effect increases with pressure, whereas the gap between these two bands decreases, given that the $^4S_{3/2}$ multiplet shifts to lower energies.

The overall pressure experiments demonstrate that detuning effects are not the main cause for UC efficiency in β-$NaYF_4$:2% Er^{3+},20%Yb^{3+} but rather is associated with crystal disorder. Although pressure slightly modifies the resonant conditions leading to neat effects on the UC luminescence intensity ratios, the structural disorder actually does guarantee resonant conditions upon crystal compression.

CONCLUSIONS

We have demonstrated multisite formation in β-$NaYF_4$:2% Er^{3+},20%Yb^{3+}, on the basis of the excitation−emission spectral dependence at low temperatures. Analogous to other family compounds, multisite emissions have also been observed in the title compound.

We have shown that the emission intensity and lifetime both decrease with pressure upon near-infrared (NIR) excitation at 978.6 nm. The intensity reduction, together with the redshift of the upconversion (UC) green emission band with pressure, make β-$NaYF_4$:2%Er^{3+},20%Yb^{3+} a reliable high-pressure low-temperature sensor.

Pressure experiments reveal that the energy gap between the $^4S_{3/2} \rightarrow {}^4I_{15/2}$ and $^2H_{11/2} \rightarrow {}^4I_{15/2}$ transitions reduces upon compression, which indicates that high-pressure effects slightly modify the electron repulsion and spin−orbit interactions being responsible for the decrease of the multiplet−multiplet separation. On the other hand, pressure additionally increases the crystal-field splitting of the Stark levels in the ground state ($^4I_{15/2}$) and excited state ($^4S_{3/2}$).

Finally, we conclude that the interplay between low phonon energy of the host lattice (∼500 cm^{-1}), multisite formation (high disordered structure), and ideal resonance conditions for Yb^{3+} ($^2F_{5/2}$)-to-Er^{3+} ($^4I_{11/2}$) energy transfer attained in β-$NaYF_4$:Er^{3+},Yb^{3+} make this material the most efficient UC phosphor ever known. Indeed, resonance conditions still remain efficient upon crystal compression, because of the multisite structure of Er^{3+}.

AUTHOR INFORMATION

Corresponding Author

*Tel.: 0034 942 201868. Fax: 0034 942 201402. E-mail: carlos.renero@unican.es.

ACKNOWLEDGMENT

This work was financially supported by the Spanish Ministerio de Ciencia e Innovación (MICINN) (under Project No. MAT2008-06873-C02-01) and by the MALTA-CONSOLIDER INGENIO 2010 Project (Ref. No. CSD2007-00045). The author also thanks the Spanish MICINN for a FPI research grant (Ref. No. BES-2009-013434).

REFERENCES

(1) Blasse, G.; Grabmaier, B.C. *Luminescent Materials*; Springer−Verlag: Berlin, 1994.
(2) Aarts, L.; van der Ende, B. M.; Meijerink, A. *Chem. Mater.* **2004**, *16*, 1–6.
(3) Valiente, R.; Millot, M.; Rodríguez, F.; González, J.; Broto, J. M.; George, S.; García-Revilla, S.; Romanyuk, Y.; Pollnau, M. *High Pressure Res.* **2009**, *29* (4), 748–753.
(4) Chivian, J. S.; Case, W. E.; Eden, D. D. *Appl. Phys. Lett.* **1979**, *35* (2), 124–125.
(5) Niedbala, R. S.; Feindt, H.; Kardos, K.; Vail, T.; Burton, J.; Bielska, B.; Shang Li; Milunic, D.; Bourdelle, P.; Vallejo, R. *Anal. Biochem.* **2001**, *293*, 22–30.
(6) Nyk, M.; Kumar, R.; Ohulchanskyy, T. Y.; Bergey, E. J.; Prasad, P. N. *Nano Lett.* **2008**, *8* (11), 3834–3838.
(7) Vetrone, F.; Naccache, R.; Juarranz de la Fuente, A.; Sanz-Rodríguez, F.; Blazquez-Castro, A.; Martín Rodriguez, E.; García Solé, J.; Capobianco, J. A. *Nanoscale* **2010**, *2*, 495–498.
(8) Vetrone, F.; Naccache, R.; Zamarrón, A.; Juarranz de la Fuente, A.; Sanz-Rodríguez, F.; Martinez Maestro, L.; Martín Rodriguez, E.; Jaque, D.; García Solé, J.; Capobianco, J. A. *ACS Nano* **2010**, *4*, 3254–3258.
(9) Sivakumar, S.; van Veggel, Frank C. J. M; Raudsepp, M. *J. Am. Chem. Soc.* **2005**, *127* (36), 12464–12465.
(10) Burns, J. H. *Ing. Chem.* **1965**, *4* (6), 881–886.
(11) Heer, S.; Kömpe, K.; Güdel, H. U.; Haase, M. *Adv. Mater.* **2004**, *16* (23−24), 2102–2105.
(12) Suyver, J. F.; Grimm, J.; van Veen, M. K.; Biner, D.; Krämer, K. W.; Güdel, H. U. *J. Lumin.* **2006**, *117*, 1–12.
(13) Aebischer, A.; Hostettler, M.; Hauser, J.; Krämer, K.; Weber, T.; Güdel, H. U.; Bürgi, H.-B. *Angew. Chem., Int. Ed.* **2006**, *45*, 2802–2806.
(14) Lage, M. M.; Moreira, R. L.; Matinaga, F. M; Gesland, J.-Y. *Chem. Mater.* **2005**, *17*, 4523–4529.
(15) Krämer, K. W.; Biner, D.; Frei, G.; Güdel, H. U.; Hehlen, M. P.; Lüthi, S. R. *Chem. Mater.* **2004**, *16*, 1244–1251.
(16) Ejder, E. *J. Opt. Soc. Am.* **1969**, *59* (2), 223–224.
(17) Grzechnik, A.; Bouvier, P.; Mezouar, M.; Mathews, M. D.; Tyagi, A. K.; Köhler, J. *J. Solid State Chem.* **2002**, *165*, 159–164.
(18) Grzechnik, A.; Bouvier, P.; Crichton, W. A.; Farina, L.; Köhler, J. *Solid State Sci.* **2002**, *4*, 895–899.
(19) Velsko, S. P.; Eimer, D. *J. Appl. Phys.* **1987**, *62*, 2461–2465.